From static to dynamic stiffness of shales: frequency and stress dependence

Serhii Lozovyi [1 2], Andreas Bauer [1 2]

[1] Norwegian University of Science and Technology, Trondheim, Norway

[2] SINTEF, Trondheim, Norway

Corresponding author – Serhii Lozovyi, e-mail: serhii.lozovyi@sintef.no

Abstract

The relation between static and dynamic stiffness in shales is important for many engineering applications. Dynamic stiffness, calculated from wave velocities, is often related to static stiffness through simple empirical correlations. The reason for this is that dynamic properties are often easier to obtain; however, it is the static properties that define the actual subsurface response to stress or pore pressure changes. Rocks are not elastic media, and stiffness depends on the stress state, stress-change amplitude, loading rate, drainage conditions, fluid saturation, and scale. All these factors require consideration when static and dynamic stiffness properties are to be related.

Two mechanisms that may have a strong effect on the stiffness of shales were studied in this experimental work: (i) a reduction of undrained static stiffness with an increase in stress amplitude and (ii) a frequency dependence (or dispersion) of dynamic stiffness. Laboratory tests were performed on four fully brine-saturated undrained field shales from different overburden formations. Experiments were conducted using a low-frequency apparatus – a triaxial loading cell with the ability to measure dynamic stiffness at seismic frequencies (1 – 150 Hz) and ultrasonic velocities (500 kHz). Shale anisotropy was characterized by testing differently oriented core plugs.

The results demonstrated that all the tested shales exhibited a dispersion of dynamic stiffness from seismic to ultrasonic frequencies. Young's modulus dispersion for the tested shales ranged from nearly 30% to above 100%. Wave velocity dispersion was on the order of 10-20% for P-waves and 20-40% for S-waves. In static tests, the undrained rock stiffness gradually decreased with increasing stress amplitude. For one shale, the static undrained Young's modulus was reduced by 50% when amplitude of the loading-unloading measurement cycle was increased from 1 MPa to 3 MPa. This finding is explained by non-elastic deformations that increase with the stress level. A method of zero-stress extrapolation of static stiffness was used to obtain the purely elastic response. The stiffness for the limit of zero stress-change amplitude agreed well with the dynamic response at seismic frequency, providing a link between static and dynamic stiffness.

Keywords

Static and dynamic moduli, Dispersion, Seismic frequencies, Shale, Anisotropy

List of Symbols

$V_{P,S}$ – velocity of shear and compressional wave, respectively, [m/s];

L – length of the rock sample, [mm];

ΔL – change in the rock sample length, [mm];

$T_{P,S}$ – total wave send-receive travel time for P- and S-waves, respectively, [s];

$T^0_{P,S}$ – correction for system travelling time, [s];

σ_{ax} – axial stress, [MPa];

A – cross section area of the sample, [mm^2];

F – axial force amplitude, [F];

$\varepsilon_{ax,\,r}$ – axial and radial strains, [mm/m];

$R_{ax,\,r}$ – amplitudes of the axial and radial strain signals, respectively, [V];

GF – gauge factor of the strain gauges, [-];

V_{in} – input voltage of the Wheatstone bridge, [V];

E, – Young's modulus, [GPa];

ν – Poisson's ratio, [-];

K, G – bulk and shear moduli, respectively, [GPa];

C_{ij} – stiffness matrix parameters, [GPa];

ε, γ, δ – Thomsen's anisotropy parameters, [-];

E_0, ν_0 – zero-stress-extrapolated Young's modulus and Poisson's ratio, [GPa, -];

E_{aver}, ν_{aver} – average Young's modulus and Poisson's ratio for the finite stress amplitude in the static test, [GPa, -];

A_{ax}, A_r – constants describing the non-elastic contribution to the static axial and radial deformation, respectively, [-].

1. Introduction

The accuracy of geomechanical modeling is greatly dependent on the rock-mechanical (or static) properties used in the model. Often, due to a lack of core material, the stiffness and strength of the rocks is estimated from dynamic elastic properties calculated from seismic or sonic wave velocities. In general, the dynamic stiffness is found to be larger than the static stiffness (King 1969; Cheng and Johnston 1981; Eissa and Kazi 1988; Martin III et al. 1994; Tutuncu et al. 1998; Fjær 2009; Sone and Zoback 2013; Yale and Swami 2017). Thus, to link static and dynamic rock-properties, empirical correlations are often used. However, those correlations do not capture all the underlaying physical processes that control rock stiffness.

As pointed out by Fjaer (2019), the most relevant causes for differences between static and dynamic moduli of rocks are strain rate, strain amplitude, drainage conditions, heterogeneities, and anisotropy. The first two factors, strain rate (or corresponding frequency for sound wave) and stress (strain) amplitude applied during loading, can result in significant errors in correlating static and dynamic elastic properties of shales (Tutuncu 2010; Holt et al. 2012, 2015). Other factors that affect static-dynamic relations should be accounted for as well. Static stiffness needs to be measured under undrained conditions since dynamic properties are derived from acoustic measurements that are also undrained. Rock anisotropy should be accounted for by measuring and comparing the same elastic stiffness parameters. One should also keep in mind that, due to heterogeneities, the dynamic wave might not represent the same rock properties as static loading caused by differences in scale.

Regarding the frequency effect, conventionally acoustic velocities in the laboratory are measured at ultrasonic frequencies (10^5 - 10^6 Hz), while in the field, velocities are measured at seismic or sonic frequencies (during seismic surveys: 1~100 Hz; sonic-log measurements in a wellbore: kHz range). Rather significant dispersion from seismic to ultrasonic frequencies has consistently been reported in shales (Suarez-Rivera et al. 2001; Duranti et al. 2005; Hofmann

2006; Tutuncu 2010; Szewczyk et al. 2018). It is believed that wave-induced (local) fluid flow in the pore space is the main mechanism for dispersion in porous rocks. The flow of the free water between adjacent pores of different shape and/or orientation occurs when the seismic wave is passing through the rock as described by, e.g., O'Connell and Budiansky (1977), Mavko and Nur (1979). Szewczyk et al. (2018) argued that the squirt flow-like mechanism is likely to occur at grain contacts involving adsorbed (bound) water, which has different properties than free water, including finite shear stiffness (Holt and Kolstø 2017).

Regarding the stress amplitude effect, a static-dynamic discrepancy is caused by the difference in stress amplitude during (quasi-)static rock compression (typically on the order of 10^{-3} m/m) and acoustic-wave propagation (typically < 10^{-6} m/m). As a result, the increase in stress-change amplitude leads to reduced stiffness. This gradual decay of stiffness with increasing stress (and strain) amplitude can be explained by a friction-controlled sliding mechanism between intergranular contacts and crack surfaces (Walsh 1965; Fjær 2009). Furthermore, (Fjær et al. 2013) have proposed a method for extrapolating rock stiffness for the limit of zero-stress change (or, respectively, zero-strain change) to find the purely elastic stiffness. This method is based on the experimental finding that the compliance of a rock (inverse of the stiffness) is a linear function of stress change during unloading. The linearity assumption has been proven to be valid down to microstrain amplitudes (Lozovyi et al. 2017). A similar method was presented by (Bilal et al. 2016). In their work, the stress-strain curves were fitted with a quadratic polynomial function, with the quadratic component representing the non-elastic contribution.

In this paper, we studied the frequency and stress amplitude effects for four different well-preserved field shales. The measurements included the undrained static stiffness, dynamic stiffness at seismic frequencies (1-150 Hz), and ultrasonic velocities (500 kHz). All shales were tested using 0°, 45° and 90° oriented cylindrical core plugs to obtain a full stiffness

characterization under the assumption that the rocks exhibit transverse isotropy (TI). We present the dependence of Young's modulus and Poisson's ratio on stress amplitude and frequency, as well as velocity dispersion plots.

2. Materials and Experimental Methods

2.1. Samples and testing procedures

In this study, three overburden shales (T, M, and B shale) and shaly facies of Opalinus Clay from Mont Terri were tested. All shales are considered fully saturated under their respective in-situ conditions. To preserve the natural saturation, shale sections were sealed immediately upon core retrieval. At SINTEF, core plugs with a diameter of 25.4 mm and length of 48-52 mm were drilled and trimmed using Marcol oil. Each shale was cored and tested at three different orientations: bedding planes perpendicular (0°), parallel (90°) and at a 45° angle to the vertical axis of the sample (Figure 1). Before the tests, T, M, and B shale plugs were stored submerged in sealed containers with Marcol oil. Opalinus Clay cores were kept in a desiccator with a relative humidity of ~93% (using a KNO_3-saturated solution) to maintain in-situ saturation according to the recommendations of Ewy (2015). The properties of the shales are shown in Table 1.

Pore pressure in the tests was applied using brines prepared according to in-situ fluid formulations. Shale cores were exposed to the synthetic brines only after drained loading to at least 4 MPa of confining pressure to prevent swelling (Ewy 2015). Further loading was performed simultaneously for pore pressure, confining pressure, and axial stress until a certain initial stress state was reached (Table 1). An example of the test protocol is shown in Figure 2. The initial stress state for the tests was chosen to mimic the in-situ net stress conditions for each rock (measurements can in principle be carried out under in-situ total stress and pore pressure, but for this study, the pore pressure was set to 2 MPa for the field shales, which is significantly less than the in-situ pore pressures, and axial and radial stresses were adjusted to provide in-

situ net stresses). For 90° and 45° oriented plugs, the mean net stress was used due to limitations of conventional triaxial pressure cells that allowed the application of only two independent stresses – radial and axial. Upon reaching the initial stress state, samples were given time consolidate before performing the measurements. In general, strain rates below 2 μstrain/h during consolidation were considered sufficiently low to have almost no effect on the shale stiffness. For Opalinus Clay, however, the elastic properties no longer changed in a significant way for a consolidation strain rate below 50 μstrain/h (Lozovyi and Bauer, 2018).

After consolidation, static stiffness measurements consisting of undrained triaxial loading-unloading sequences with stress magnitudes of up to 5 MPa were performed (Figure 2). Dynamic measurements included ultrasonic frequency (500 kHz) and low frequencies (1-150 Hz). Ultrasonic velocities were recorded continuously during the whole test. Low-frequency measurements were conducted only after consolidation at the initial stress state. Good coupling of the sample and pistons was needed for the low-frequency measurement. Therefore, for some tests in which consolidation and static measurement were performed under isostatic stress conditions (i.e., Opalinus Clay, and 90° and 45° oriented plugs for other shales), axial deviatoric stress of 1 MPa was applied followed by an additional consolidation period. All tests were performed at room temperature.

[Table 1]

[Figure 1- Figure 2]

2.2. Experimental setup

SINTEF's low-frequency apparatus was used in this study. In this section, a brief description of the apparatus and the principles of the low-frequency measurement will be presented. For more comprehensive information, see Szewczyk et al. (2016), Lozovyi and Bauer (2019). We also refer to an overview of the low-frequency technique by Subramaniyan et al. (2014).

The low-frequency apparatus used in this work is a custom-built triaxial cell that was designed for measurements of undrained dynamic elastic moduli of rock specimens at seismic frequencies (0.1-155 Hz), as well as ultrasonic P- and S-wave velocities (500 kHz) under various stress conditions, with independent control of axial stress, radial stress and pore pressure (see Figure 3).

Ultrasonic measurements were performed by the standard pulse-transmission technique. P- and S-wave piezo-electric transducers with a central frequency of 500 kHz were mounted inside the titanium endcaps. This configuration allows the measurement of ultrasonic velocities along the sample's vertical axis. The velocities are given by

$$V_{P,S} = \frac{L - \Delta L}{T_{P,S} - T^0_{P,S}}, \quad (1)$$

where L is the initial length of the sample, ΔL – the change in sample length as a result of applied stresses, $T_{P,S}$ – the total wave send-receive travel time for the P- and S-wave, respectively, and $T^0_{P,S}$ – the correction for system travel time for P- and S-waves, respectively.

The low-frequency measurements can directly provide dynamic elastic parameters, Young's modulus and Poisson's ratio, within the seismic band (0.1-155 Hz). The difficulty of the measurement is that strain-modulation amplitudes are kept below 10^{-6} to stay in the elastic regime (for higher strain amplitudes, the dynamic stiffness is impacted by non-elastic effects, see Winkler et al. 1979; Batzle et al. 2006; Lozovyi et al. 2017. Thus, the sample is excited in the axial direction by a piezo-electric displacement actuator, which is placed in a column of the elements in the cell (see Figure 3a). It creates very small and precise deformations in the axial direction as the piezo element elongates and contracts. The actuator is controlled by a continuous sinusoidal signal. The resulting force modulation is measured by a piezoelectric force sensor. The amplitude and phase of the force signal are measured by a lock-in amplifier and continuously acquired using specially developed software.

The stress amplitude (σ_{ax}) is calculated from the force amplitude (F) and the cross section of the sample (A):

$$\sigma_{ax} = \frac{F}{A} \ . \tag{2}$$

The strain modulations are measured by strain gauges attached to the sample surface (Figure 3b). Eight strain gauges (four radial and four axial) are connected to four Wheatstone bridges with the half-bridge configuration in such a way that the strains on the opposite sides of the sample are averaged by the bridge.

The voltage signals from the Wheatstone bridges are analyzed by four additional lock-in amplifiers (two for axial and two for radial strain signals). The amplifiers provide the amplitudes and phases of the signals. The axial (ε_{ax}) and radial (ε_r) strains are calculated by

$$\varepsilon_{ax,r} = \frac{2R_{ax,r}}{V_{in} \times GF} \ , \tag{3}$$

where R_{ax} and R_r are the amplitudes of the axial and radial strains, respectively, and GF – is the gauge factor of the strain gauges.

Typical signals of axial stress as well as axial and radial strains during the low-frequency measurement are shown on Figure 4. Young's modulus (E) and Poisson's ratio (ν) can be calculated directly by

$$E = \frac{\sigma_{ax}}{\varepsilon_{ax}}; \nu = -\frac{\varepsilon_r}{\varepsilon_{ax}} \ . \tag{4}$$

For isotropic homogeneous materials, only two independent stiffness parameters are needed to define the elastic properties. The other moduli, such as bulk modulus (K) and shear modulus (G), can be calculated as follows:

$$K = \frac{E}{3(1-2\nu)}; G = \frac{E}{2(1+\nu)} \ . \tag{5}$$

The shales used in this study were assumed to be transverse isotropic (TI). TI media are characterized by five independent stiffness parameters (see section 3). Low-frequency measurements were performed under uniaxial stress conditions along the sample axis. Therefore, measurements for at least three samples with different orientations had to be performed (Figure 1). In this way, stress was applied along, perpendicular and at 45 degrees to the symmetry axis of the medium. Young's moduli, E_V, E_H and E_{45}, are obtained from respective 0°, 90° and 45° oriented samples by measuring stresses and strains along the sample axis. Poisson's ratio, ν_{VH}, was obtained with 0°-oriented samples as a ratio of the radial to axial strains. Another two Poisson's ratios, ν_{HV} and ν_{HH}, were obtained with the 90° sample as ratios of the two orthogonal principal radial strains (see Figure 1) to the axial strain. Here, the first index denotes the direction of uniaxial stress (V – vertical, along symmetry axis, H – horizontal, perpendicular to the symmetry axis), and the second index represents the direction of transverse strain.

[Figures 3-4]

3. Data Analysis

In the low-frequency cell, three different sets of rock properties were obtained from static, seismic (low frequency) and ultrasonic measurements. Young's and bulk moduli and Poisson's ratios were obtained in static cycles, the low-frequency technique provided dynamic Young's moduli and Poisson's ratios, and the ultrasonic technique gave P- and S-wave velocities. Table 2 shows the difference between different types of measurements in terms of frequency (or strain rate) and strain amplitude. The low-frequency measurements of the seismic frequency band together with ultrasonic measurements allowed the study of the dispersion, i.e., the frequency dependence of stiffness and velocities. While dynamic measurements were performed at very low strain amplitudes, static measurements involved much higher strains. This process allowed the quantification of the stress dependent non-elastic contribution to rock

deformations. Typical strain rates of static measurement were on the same scale of magnitude as a strain rate used in low-frequency measurements, so if other conditions were similar (e.g., stress/strain amplitudes, drainage conditions), static stiffness should be equal to the dynamic at this point.

A comparison of the obtained results requires conversion between the different parameters. This chapter will describe the conversion between elastic parameters, transversely isotropic (TI) stiffness matrix coefficients, and wave velocities.

Shales are conventionally considered transversely isotropic media. A stiffness tensor of a TI medium contains five independent stiffness parameters and can be written in the form of a 6×6 matrix (using Voigt notation; Nye, 1984):

$$\vec{\sigma} = \begin{pmatrix} C_{11} & C_{11}-2C_{66} & C_{13} & 0 & 0 & 0 \\ C_{11}-2C_{66} & C_{11} & C_{13} & 0 & 0 & 0 \\ C_{13} & C_{13} & C_{33} & 0 & 0 & 0 \\ 0 & 0 & 0 & C_{44} & 0 & 0 \\ 0 & 0 & 0 & 0 & C_{44} & 0 \\ 0 & 0 & 0 & 0 & 0 & C_{66} \end{pmatrix} \cdot \vec{\varepsilon} \ . \tag{6}$$

Here, C_{11}, C_{33}, C_{44}, C_{66}, and C_{13} are five independent stiffness parameters.

The stiffness parameters relate to wave velocities as follows:

$$\begin{aligned} \rho \mathrm{v}_{PV}^2 &= C_{33}, \\ \rho \mathrm{v}_{PH}^2 &= C_{11}, \\ \rho \mathrm{v}_{SV}^2 &= C_{44}, \\ \rho \mathrm{v}_{SH}^2 &= C_{66}. \end{aligned} \tag{7}$$

Here, V_{PV} and V_{PH} denote velocities of P-waves perpendicular and parallel to bedding, respectively, V_{SV} is the S-wave velocity for waves travelling perpendicular to bedding, and V_{SH} is the S-wave velocity for waves travelling parallel to bedding with polarization within the bedding plane.

Rock anisotropy can be quantified by three unitless parameters introduced by Thomsen (1986):

$$\varepsilon = \frac{C_{11} - C_{33}}{2C_{33}}$$
$$\gamma = \frac{C_{66} - C_{44}}{2C_{44}} \quad (8)$$
$$\delta = \frac{(C_{13} + C_{44})^2 - (C_{33} - C_{44})^2}{2C_{33}(C_{33} - C_{44})}$$

ε can be interpreted as the P-wave anisotropy and γ as the S-wave anisotropy. δ is the so-called moveout parameter, and together with ε, it controls the anellipticity of the P-wavefront.

3.1. Static measurements

For rock with TI symmetry, static measurements must be performed for three different sample orientations (when only axial and confining stresses are controlled independently). In this study, however, static properties for most of the shales were only obtained for 0° samples, so that only 3 out of 5 independent stiffness parameters could be determined. Nevertheless, we could link static Young's moduli and Poisson's ratios (relevant parameters for geomechanical simulations) to their dynamic counterparts at seismic and ultrasonic frequencies. It should be noted that static properties of B shale were not tested.

3.2. Dynamic measurements

The following elastic 6 parameters were measured at seismic frequencies with the following sample orientations: 0° sample – E_V, ν_{VH}; 90° sample – E_H, ν_{HV}, ν_{HH}; 45° sample – E_{45}. The measured moduli can be converted into stiffness matrix parameters according to (Bower 2010):

$$
\begin{aligned}
C_{11} &= E_H(1-\nu_{HV}\nu_{VH})\Lambda, \\
C_{33} &= E_V(1-\nu_{HH}^2)\Lambda, \\
C_{13} &= E_H\nu_{VH}(1+\nu_{HH})\Lambda, \\
C_{44} &= \left(\frac{4}{E_{45}}-\frac{1}{E_V}-\frac{1}{E_H}+\frac{C_{13}}{(C_{11}-C_{66})C_{33}-C_{13}^2}\right)^{-1}, \\
C_{66} &= E_H/2(1+\nu_{HH}), \\
\Lambda &= \left(1-\nu_{HH}^2-2\nu_{HV}\nu_{VH}-2\nu_{HV}\nu_{VH}\nu_{HH}\right)^{-1}.
\end{aligned}
\tag{9}
$$

Additionally, for TI symmetry, it can be shown that (Holt 2016)

$$
\left(\frac{E_V}{E_H}\right)\Big/\left(\frac{\nu_{VH}}{\nu_{HV}}\right)=1. \tag{10}
$$

Deviations from unity of the left term in Equation 10 will indicate deviations from TI symmetry or differences in properties of 0° and 90°-oriented samples caused by heterogeneities in the rock.

As shown above, the low-frequency setup allowed the measurement of six elastic parameters, meaning that one parameter in redundant. A least-squares fit routine was used to constrain the 5 independent stiffness parameters from the 6 measured parameters. For fit, the relative error of Poisson's ratios was assumed to be twice as high as that of Young's moduli, since Poisson's ratio was calculated from two strain-gauge signals while Young's moduli were calculated from one strain-gauge signal only, and the errors of the strain-gauge signals were the dominant error sources.

The estimated error in the P-wave modulus (C_{33}) derived from measurements at seismic frequencies could be up to 20% depending on the rock. This would result in up to 10% error in the corresponding P-wave velocity. Young's moduli and Poisson's ratios, in turn, could be measured with absolute uncertainty of ~5%.

The measured ultrasonic velocities had an error of less than 1%. The uncertainty in the inverted dynamic Young's moduli and Poisson's ratios from P- and S-wave ultrasonic velocities measured in the axial direction for 0°, 45°, and 90°-oriented samples (using equations 3 and 5)

could be up to 10%, depending on the degree of rock heterogeneity. The error was particularly sensitive to uncertainties in velocity measured with the 45° sample.

4. Results

In total, four sets of experiments were carried out (with T, M, B shales, and Opalinus Clay), with each set consisting of 3 tests with differently oriented samples (0°, 45°, and 90°) cored from the same core section.

4.1. Non-elastic effects

For T and M shales, as well as Opalinus Clay, the effect of stress amplitude on non-elastic effects was studied in undrained triaxial loading-unloading cycles. Here, by non-elastic deformations, we mean the hysteresis that is observed in stress-strain curves for a full unloading-loading cycle; non-elastic in this context does not mean plastic since, for at least several stress cycles, the same stress and strain state is reached upon completion of the cycle[1]. The loading cycles were performed after the samples were consolidated at the respective reference stress states (see Table 1).

Among the tested shales, Opalinus Clay exhibited the strongest non-elasticity effects (hysteresis in stress-strain curves). Figure 5 shows the axial and radial strain as a function of stress change for the different undrained triaxial loading/unloading cycles. In the first cycle, the axial stress was increased by 1 MPa and in the second cycle by 3 MPa (loading rate 5 MPa/h). We observed strong non-linearity in the stress-strain relation, which increased with increasing stress magnitude.

To quantify the non-elastic effects, we applied the model by (Fjær et al. 2013). We plotted the incremental axial compliances, $d\varepsilon_{ax}/d\sigma_{ax}$ and $d\varepsilon_{rad}/d\sigma_{ax}$, as a function of stress

[1] Plastic, non-reversable rock deformations may occur during the first loading cycle, those plastic deformations are not subject of the present study.

change, $\Delta\sigma_{ax}$, during the unloading sequences (Figure 6). The compliance was low in the beginning and increased gradually as the stress change increased. The linearity of the compliance function was in agreement with previous measurements with sandstones and shales (Fjær et al. 2013; Lozovyi et al. 2017). The slope of the compliance function is a measure of non-elasticity: a steeper slope indicates a stronger non-elastic contribution to the stress-strain relation.

Interestingly, the non-elastic contribution was almost absent for T shale; for M shale, we observed an intermediate non-elasticity (Figure 6). For both T and M shales, the stress amplitude of the triaxial undrained static cycles was ~5 MPa. We observed a linear dependence of the incremental compliance in all measurements for both axial and radial strains.

[Figures 5-6]

The dependence of rock stiffness on stress change can be described by a semiempirical model. By assuming linear relationships between incremental compliances (both $d\varepsilon_{ax}/d\sigma_{ax}$ and $d\varepsilon_{rad}/d\sigma_{ax}$) and axial-stress change, the average compliances can be expressed in the following way (Lozovyi et al. 2017):

$$\frac{\Delta\varepsilon_{ax}}{\Delta\sigma_{ax}} = \frac{1}{E_{aver}(\Delta\sigma_{ax})} = \frac{A_{ax}\cdot\Delta\sigma_{ax}}{2} + \left(\frac{d\varepsilon_{ax}}{d\sigma_{ax}}\right)_0 \tag{11}$$

$$\frac{\Delta\varepsilon_{r}}{\Delta\sigma_{ax}} = \frac{A_{r}\cdot\Delta\sigma_{ax}}{2} + \left(\frac{d\varepsilon_{r}}{d\sigma_{ax}}\right)_0 \tag{12}$$

Here, A_{ax} and A_r are constants, and $(d\varepsilon_{ax}/d\sigma_{ax})_0$ and $(d\varepsilon_r/d\sigma_{ax})_0$ are the zero-stress extrapolated compliances, with $(d\varepsilon_{ax}/d\sigma_{ax})_0$ being the inverse of the zero-stress extrapolated Young's modulus, $1/E_0$. The average Poisson's ratio, ν, is obtained by dividing Eq. 12 by Eq. 11: $\nu_{aver} = -(\Delta\varepsilon_r/\Delta\sigma_{ax})/(\Delta\varepsilon_{ax}/\Delta\sigma_{ax})$. The zero-stress extrapolated Poisson's ratio is accordingly given by $\nu_0 = -(d\varepsilon_r/d\sigma_{ax})_0/(d\varepsilon_{ax}/d\sigma_{ax})_0$.

For example, of Opalinus Clay, we demonstrated how strongly the stiffness could be affected by the amplitude of the stress change (Figure 7). Here, the A_{ax} and A_r parameters (see Eqs. 11 and 12) were determined (and averaged) from the stress-strain data for the 1 and 3 MPa unloading sequences shown in Figure 5. Solid lines in Figure 7 represent modeled stiffness, while red points show measured values.

[Figure 7]

4.2. Dispersion

Low-frequency and ultrasonic measurements provided information about the dispersion of dynamic rock stiffness and velocities between seismic and ultrasonic frequencies. The dynamic measurements were performed under the same initial stress conditions (Table 1) as static tests (except for Opalinus Clay, where the deviatoric stress was increased to 1 MPa). The measurements were performed with 0°, 45°, and 90°-oriented samples of T, M, and B shale, and Opalinus Clay. At low frequencies, Young's moduli and Poisson's ratios were measured directly with differently oriented samples, as shown on Figure 1. Ultrasonic P- and S-wave velocities were measured along the sample axis for each of the three sample orientations. Both low-frequency and ultrasonic measurements allowed for a full TI-stiffness characterization for the different shale types, i.e., all 5 independent stiffness parameters (C_{ij}) obtained for both seismic frequencies (1-150 Hz) and ultrasonic frequencies (500 kHz) as described in Chapter 3. Figure 8 shows C_{ij} parameters as a function of frequency for the four tested shales. From the stiffness matrix C_{ij} together with the rock density, wave velocities for any propagation angle could be calculated.

[Figure 8]

The corresponding Thomsen's anisotropy parameters are plotted in Figure 9 as functions of frequency.

[Figure 9]

4.3. Non-elastic effects and dispersion combined

Figure 10 shows the frequency dependence of Young's moduli and Poisson's ratios obtained from low-frequency measurements at seismic and ultrasonic frequencies (circles), and quasi-static measurements (unloading sequences). It is important to note that Young's moduli and Poisson's ratios were directly measured in quasi-static and low-frequency measurements, while for ultrasonic measurements, Young's moduli and Poisson's ratios were inverted from P- and S-wave velocities measured in the axial direction for 0°, 45°, and 90° oriented samples (using Equations 7 and 9).

The quasi-static measurements were carried out with a certain loading rate (or strain rate), which can be related to a frequency of a stress (strain) modulation for which the average stress (strain) rate is the same as for the unloading sequence of the quasi-static measurement (Fjær et al. 2013). In our case, the loading rate of 5 MPa/h corresponded to subhertz frequencies. The quasi-static stiffness data shown in Figure 10 include the average Young's moduli and Poisson's ratios (orange symbols) and the corresponding zero-stress extrapolated values (green symbols), as discussed in Chapter 4.1, as well as the average Young's moduli and Poisson's ratios obtained from stress and strain relations that include deformations (creep) during their consolidation phase after completion of unloading (indicated by red arrows pointing to lower frequencies). An example of creep after undrained loading and unloading sequences is shown in Figure 5. Obviously, the static moduli calculated from strains that included creep consolidation were lower than the moduli obtained from the stress-strain curves recorded during

the unloading sequences. For all shales studied, the zero-stress extrapolated static stiffness (unloading sequences of triaxial cycles) was close to the dynamic stiffness at 1 Hz.

[Figure 10]

5. Discussion

To better evaluate the relation between static and dynamic Young's moduli and Poisson's ratios, the experimental data for T, M, and B shale, and Opalinus Clay are summarized in Table 3. It should be noted that no static data were available for B shale. Additionally, in the absence of ultrasonic S-wave measurements for the 90° sample of B shale due to technical problems, the ultrasonic Young's modulus and Poisson's ratio were derived under some assumption and might result in larger errors than stated in Section 3.2. Table 3 also provides ratios between seismic and static, ultrasonic and seismic, and ultrasonic and static stiffness. The static undrained stiffness was measured for $\Delta\sigma_{ax} \approx 5$ MPa with M and T shales, and for $\Delta\sigma_{ax} = 3$ MPa with Opalinus Clay.

The results demonstrated that all shales exhibited a large dispersion of Young's modulus, E_V between seismic and ultrasonic frequencies, ranging from approximately 30% for T shale to approximately 110% for Opalinus Clay. Considerable dispersion was also observed for Poisson's ratio.

Table 4 summarizes P- and S-wave velocities in principal directions for seismic and ultrasonic frequencies. P-wave velocity dispersion appeared to be much less prominent than for elastic parameters; it varied from 2% to 25% for the different shales. S-wave velocity dispersion was generally higher, ranging from 15% to 44%. It was evident that the overburden shales (B, M, and T shales) exhibited a similar level of seismic dispersion, whereas Opalinus Clay was notably more dispersive. The exact mechanisms underlying seismic dispersion in shales are not

fully understood. Presumably, dispersion is mostly caused by a local fluid flow and bound-water relaxation process (Szewczyk et al. 2018).

The variation of non-elastic effects on the static stiffness for different shales was even larger than the variation in dispersion: for T shale, non-elastic effects were almost absent (3% difference between static and seismic Young's modulus), and the shale exhibited a nearly perfect elastic response for stress changes up to at least 5 MPa; M shale showed intermediate non-elastic contributions to the stiffness (29% difference between static and seismic Young's modulus); and Opalinus Clay exhibited very large non-elastic contributions – its static stiffness was heavily affected by the change in vertical stress (80% reduction in E_V for $\Delta\sigma_{ax}$ = 3 MPa). For all shales, however, the zero-stress extrapolated static undrained stiffness agreed well with the dynamic stiffness at low frequency. It represented pure elastic stiffness. The often smaller static (undrained) stiffness compared to dynamic stiffness measured with seismic, sonic, or ultrasonic methods is likely due to the occurrence of non-elastic processes during both unloading or loading.

[Tables 3 - 4]

The strong difference in non-elastic deformations between T shale (nearly perfectly elastic) and Opalinus Clay (highly non-elastic) could possibly be attributed to the overconsolidation ratio and the magnitude of the present-day in situ effective stress. It is known that Opalinus Clay has experienced strong uplift by approximately 900 m (Bossart 2011). T shale, in contrast, is a deeply buried shale. It is possible that cracks were formed during uplift and stress release. These cracks may act as sliding surfaces, contributing to non-elastic processes during stress changes, as described by Fjær et al. (2013).

The observation that Opalinus Clay and T shale showed a similar order of seismic dispersion but exhibit a largely different non-elastic response upon unloading and loading

suggests that the mechanisms responsible for dispersion are different from the mechanisms responsible for non-elastic processes.

6. Conclusions

In this work, a systematic experimental study was carried out with the aim of identifying processes that can link the static and dynamic stiffness of shales under undrained conditions. A particular focus was the frequency and stress-amplitude effects. The measurements of four field shales included undrained quasi-static loading cycles from which the static stiffness was derived, dynamic stiffness measurement at seismic frequencies (1 – 150 Hz), and ultrasonic velocity measurements. The obtained results demonstrate that the difference between static and dynamic stiffness in shales is due to both dispersion and stress-amplitude-dependent non-elastic effects. The dispersion mechanism was the most prominent for Young's modulus: for the tested shales, Young's modulus increased by 30% to more than 100% from seismic to ultrasonic frequencies. P-wave velocity dispersion was observed on the order of 10-20% between seismic and ultrasonic frequencies. In the stress cycles, non-elastic deformations were found to increase with increasing stress-change amplitude, resulting in a reduction of the rock stiffness. The largest stress-amplitude effect was observed for Opalinus Clay: the average static undrained Young’s modulus, measured for a stress amplitude of 3 MPa, was 50% lower than that measured for a 1 MPa stress cycle. A method of zero-stress extrapolation of static stiffness was used to obtain the purely elastic response from undrained static experiments. The zero-stress extrapolated stiffness agreed well with the dynamic response at seismic frequency, providing a link between the static and dynamic stiffness. It is important to note the absence of a constant factor between static and dynamic stiffness, as is often assumed when estimating static stiffness from sonic and seismic data. Instead, the static stiffness of shales strongly depends on the amplitude of the stress change, which should be taken into account when building geomechanical models.

7. Acknowledgments

The authors acknowledge financial support from the Research Council of Norway and industrial partners in the following consortia:

- Shale Rock Physics 2 with AkerBP, INEOS, ENGIE, Maersk and Total (Grant 234074)
- Improved Prediction of Stress and Pore-pressure Changes in the Overburden for Infill Drilling with AkerBP, Equinor and Shell (Grant 294369).

The authors also acknowledge Dr. Silvio Giger from NAGRA for providing information about the Opalinus Clay and sample preparation, as well as several helpful discussions. BP is acknowledged for providing core material and support. The two anonymous reviewers are thanked for their constructive comments.

8. References

Batzle ML, Han D-H, Hofmann R (2006) Fluid mobility and frequency-dependent seismic velocity — Direct measurements. GEOPHYSICS 71:N1–N9. doi: 10.1190/1.2159053

Bilal A, Myers MT, Hathon LA (2016) An Investigation of Static and Dynamic Data Using Multistage Tri-Axial Test. American Rock Mechanics Association

Bossart P (2011) Characteristics of the Opalinus Clay at Mont Terri

Bower AF (2010) Applied mechanics of solids. CRC Press, Boca Raton

Cheng CH, Johnston DH (1981) Dynamic and static moduli. Geophys Res Lett 8:39–42. doi: 10.1029/GL008i001p00039

Duranti L, Ewy R, Hofmann R (2005) Dispersive and attenuative nature of shales: multiscale and multifrequency observations. In: 75th Annual International Meeting. Society of Exploration Geophysicists, pp 1577–1580

Eissa EA, Kazi A (1988) Relation between static and dynamic Young's moduli of rocks. In: International Journal of Rock Mechanics and Mining Sciences & Geomechanics Abstracts. Elsevier, pp 479–482

Ewy RT (2015) Shale/claystone response to air and liquid exposure, and implications for handling, sampling and testing. Int J Rock Mech Min Sci 80:388–401. doi: 10.1016/j.ijrmms.2015.10.009

Fjær E (2009) Static and dynamic moduli of a weak sandstone. GEOPHYSICS 74:WA103–WA112. doi: 10.1190/1.3052113

Fjaer E (2019) Relations between static and dynamic moduli of sedimentary rocks: Relations between static and dynamic moduli. Geophys Prospect 67:128–139. doi: 10.1111/1365-2478.12711

Fjær E, Stroisz AM, Holt RM (2013) Elastic Dispersion Derived from a Combination of Static and Dynamic Measurements. Rock Mech Rock Eng 46:611–618. doi: 10.1007/s00603-013-0385-8

Hofmann R (2006) Frequency dependent elastic and anelastic properties of clastic rocks

Holt R (2016) Bounds of elastic parameters characterizing transversely isotropic media: Application to shales. GEOPHYSICS 81:C243–C252. doi: 10.1190/geo2015-0485.1

Holt RM, Bauer A, Fjær E, et al (2015) Relating Static and Dynamic Mechanical Anisotropies of Shale. American Rock Mechanics Association

Holt RM, Kolstø MI (2017) How does water near clay mineral surfaces influence the rock physics of shales? Geophys Prospect 65:1615–1629. doi: 10.1111/1365-2478.12503

Holt RM, Nes O-M, Stenebraten JF, Fjær E (2012) Static vs. dynamic behavior of shale. In: 46th US Rock Mechanics/Geomechanics Symposium. American Rock Mechanics Association

King MS (1969) Static and dynamic elastic moduli of rocks under pressure. pp 329–351

Lozovyi S, Bauer A (2018) Static and dynamic stiffness measurements with Opalinus Clay. Geophys Prospect. doi: 10.1111/1365-2478.12720

Lozovyi S, Bauer A (2019) Velocity dispersion in rocks: A laboratory technique for direct measurement of P-wave modulus at seismic frequencies. Rev Sci Instrum 90:024501. doi: 10.1063/1.5026969

Lozovyi S, Sirevaag T, Szewczyk D, et al (2017) Non-Elastic Effects in Static and Dynamic Rock Stiffness. In: 51st US Rock Mechanics/Geomechanics Symposium. American Rock Mechanics Association

Martin III RJ, Haupt RW, others (1994) Static and dynamic elastic moduli in granite: The effect of strain amplitude. In: 1st North American Rock Mechanics Symposium. American Rock Mechanics Association, pp 473–480

Mavko GM, Nur A (1979) Wave attenuation in partially saturated rocks. GEOPHYSICS 44:161–178. doi: 10.1190/1.1440958

Nye JF (1985) Physical properties of crystals: their representation by tensors and matrices. Oxford University Press

O'Connell RJ, Budiansky B (1977) Viscoelastic properties of fluid-saturated cracked solids. J Geophys Res 82:5719–5735. doi: 10.1029/JB082i036p05719

Sone H, Zoback MD (2013) Mechanical properties of shale-gas reservoir rocks — Part 1: Static and dynamic elastic properties and anisotropy. GEOPHYSICS 78:D381–D392. doi: 10.1190/geo2013-0050.1

Suarez-Rivera R, Willson SM, Nakagawa S, Magnar-Ness O (2001) Frequency Scaling for Evaluation of Shale and Mudstone Properties from Acoustic Velocities. AGU Fall Meet Abstr 32:

Subramaniyan S, Quintal B, Tisato N, et al (2014) An overview of laboratory apparatuses to measure seismic attenuation in reservoir rocks: Apparatuses to measure seismic attenuation. Geophys Prospect 62:1211–1223. doi: 10.1111/1365-2478.12171

Szewczyk D, Bauer A, Holt RM (2016) A new laboratory apparatus for the measurement of seismic dispersion under deviatoric stress conditions. Geophys Prospect 64:789–798. doi: 10.1111/1365-2478.12425

Szewczyk D, Holt RM, Bauer A (2018) The impact of saturation on seismic dispersion in shales — Laboratory measurements. GEOPHYSICS 83:MR15–MR34. doi: 10.1190/geo2017-0169.1

Thomsen L (1986) Weak elastic anisotropy. GEOPHYSICS 51:1954–1966. doi: 10.1190/1.1442051

Tutuncu AN (2010) Anisotropy, Compaction And Dispersion Characteristics of Reservoir And Seal Shales. In: 44th U.S. Rock Mechanics Symposium and 5th U.S.-Canada Rock Mechanics Symposium, 27-30 June, Salt Lake City, Utah

Tutuncu AN, Podio AL, Gregory AR, Sharma MM (1998) Nonlinear viscoelastic behavior of sedimentary rocks, Part I: Effect of frequency and strain amplitude. GEOPHYSICS 63:184–194. doi: 10.1190/1.1444311

Walsh JB (1965) The effect of cracks on the uniaxial elastic compression of rocks. J Geophys Res 70:399–411. doi: 10.1029/JZ070i002p00399

Winkler K, Nur A, Gladwin M (1979) Friction and seismic attenuation in rocks. Nature 277:528–531. doi: 10.1038/277528a0

Yale DP, Swami V (2017) Conversion of Dynamic Mechanical Property Calculations to Static Values for Geomechanical Modeling. In: 51st US Rock Mechanics/Geomechanics Symposium. American Rock Mechanics Association

Figures

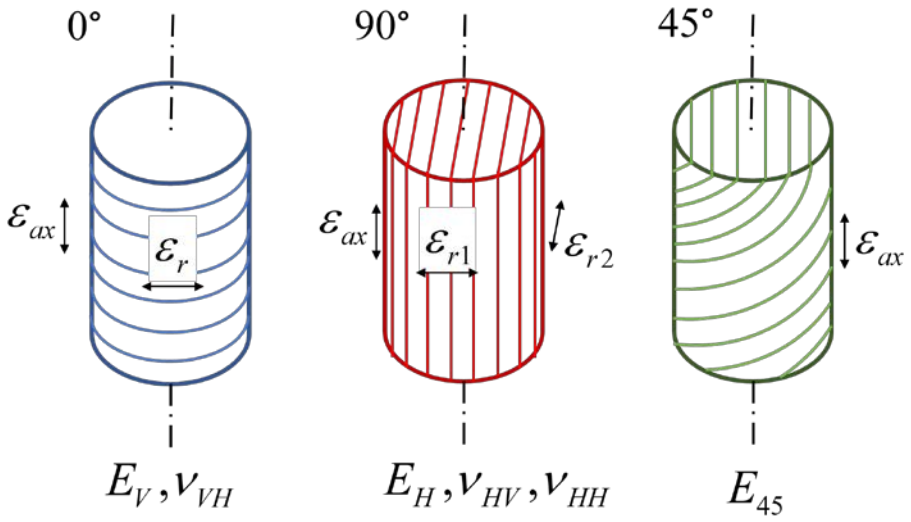

Figure 1. Sample orientations (0°, 90°, and 45°) and corresponding strains (ε) and stiffness parameters (Young's moduli, E, and Poisson's ratios, ν) that are measured with the low frequency technique for transversely isotropic samples.

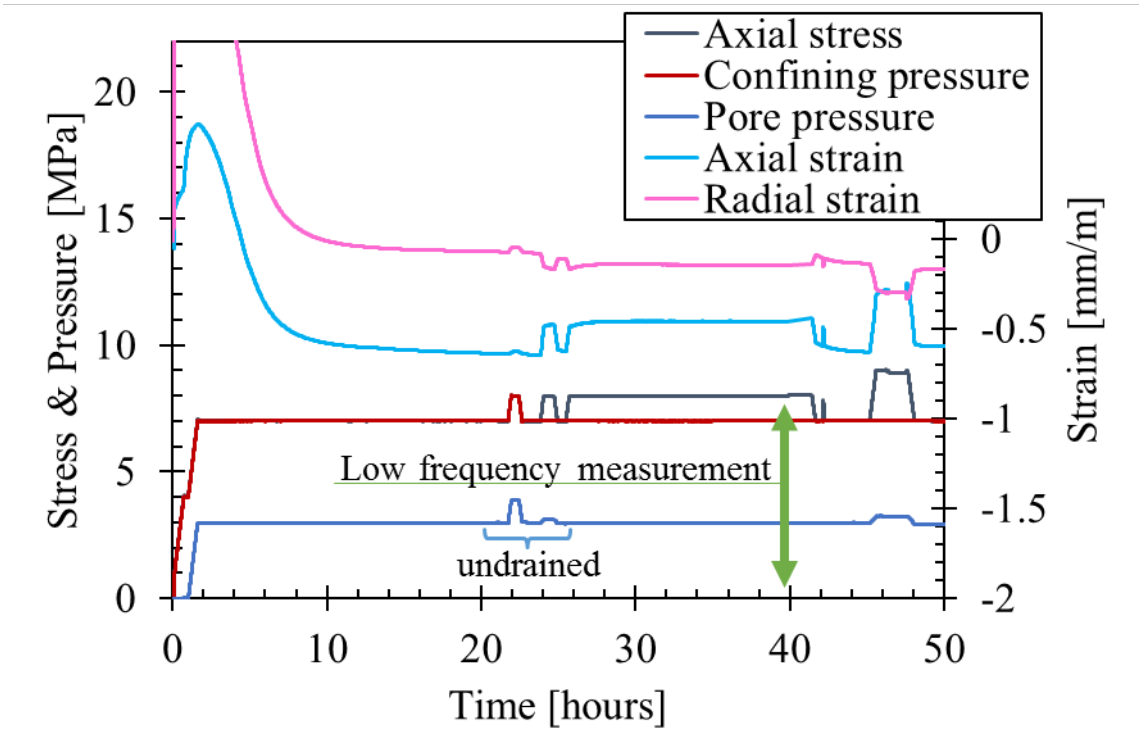

Figure 2. Test protocol of shale experiments in the low-frequency cell (an example of Opalinus Clay). Confining pressure is first increased to 4 MPa, and then pore and confining pressures are raised simultaneously to the in-situ net stress level. Note that here swelling is observed when the sample comes in

contact with pore fluid. After the consolidation period, static undrained loading cycles are performed to obtain the static stiffness. For the low-frequency measurement, deviatoric stress is increased to 1 MPa, and the measurement is performed after consolidation. In this test, an additional 3 MPa static cycle was run at the end. Ultrasonic P- and S-wave velocities are recorded during the whole test.

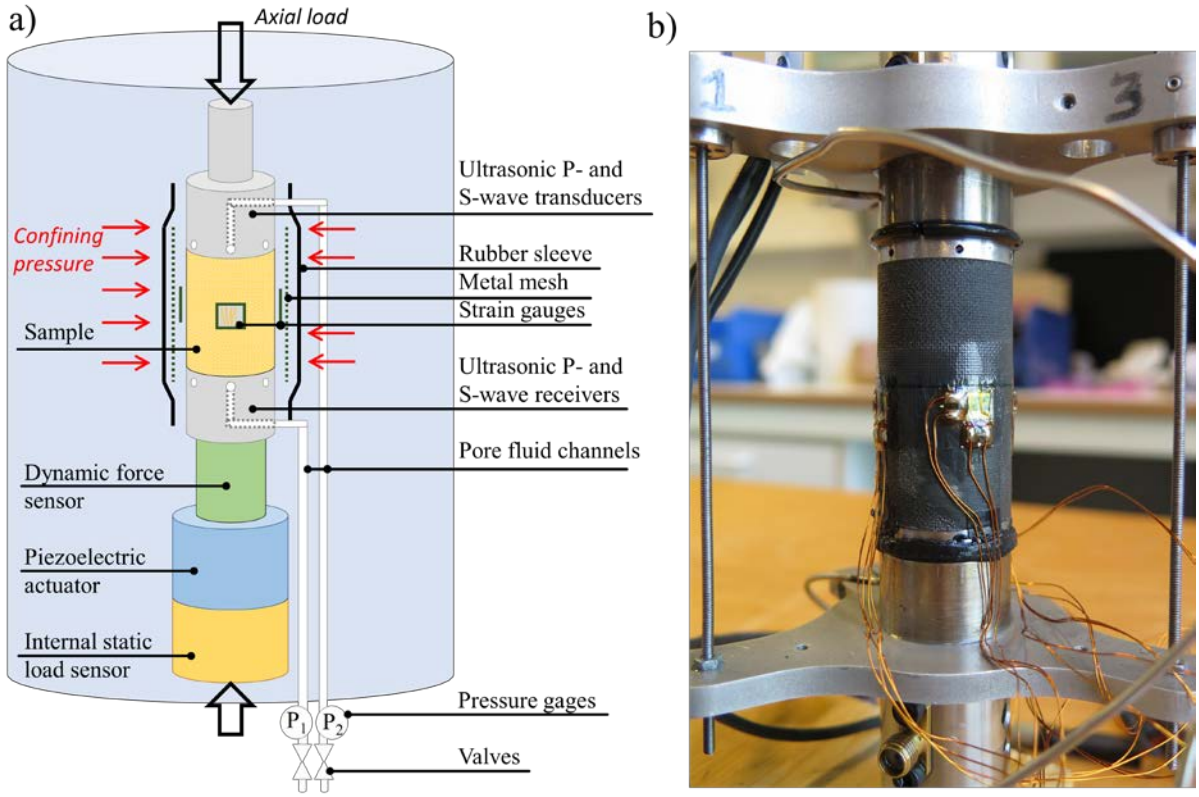

Figure 3. The low-frequency apparatus at the SINTEF formation physics laboratory in Norway: a) schematic of the apparatus; b) photograph of the sample mounted between endcaps with the rubber sleeve removed after the test.

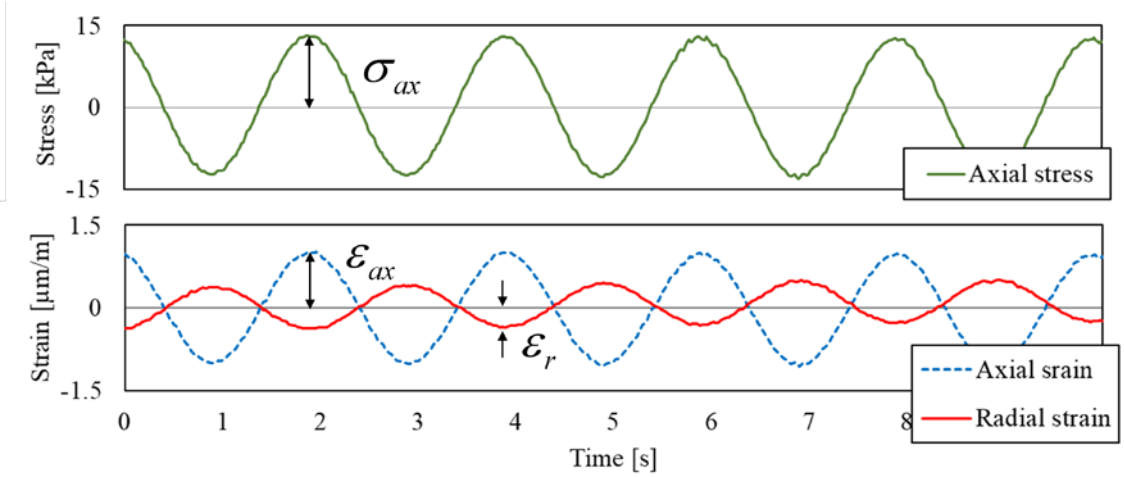

Figure 4. Recorded measurements of axial stress (σ_{ax}), axial (ε_{ax}) and radial (ε_r) strain oscillation during the low-frequency measurement at a frequency of 0.5 Hz.

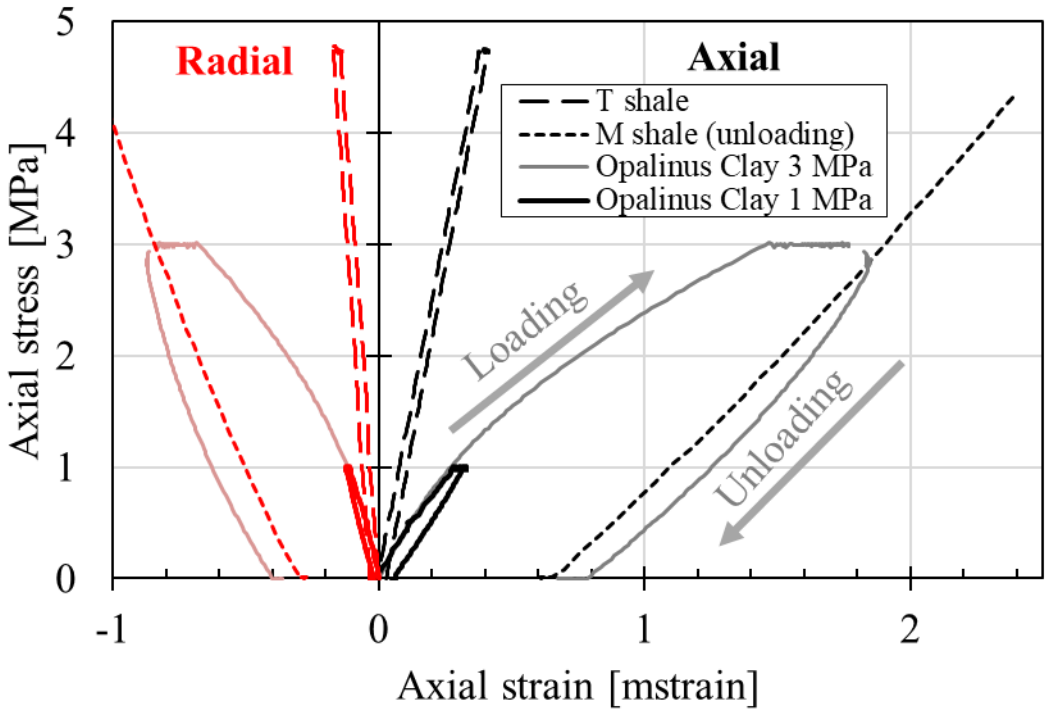

Figure 5. Axial and radial strain increments ($\Delta\varepsilon$) as functions of the axial stress increment ($\Delta\sigma_{ax}$) acquired with T, M shales and Opalinus Clay during undrained triaxial loading cycles. Opalinus Clay was tested with two stress amplitudes of 1 MPa and 3 MPa. T, M shales were tested in almost 5 MPa cycles. Note, only unloading data was recorded for M shale due to technical issues.

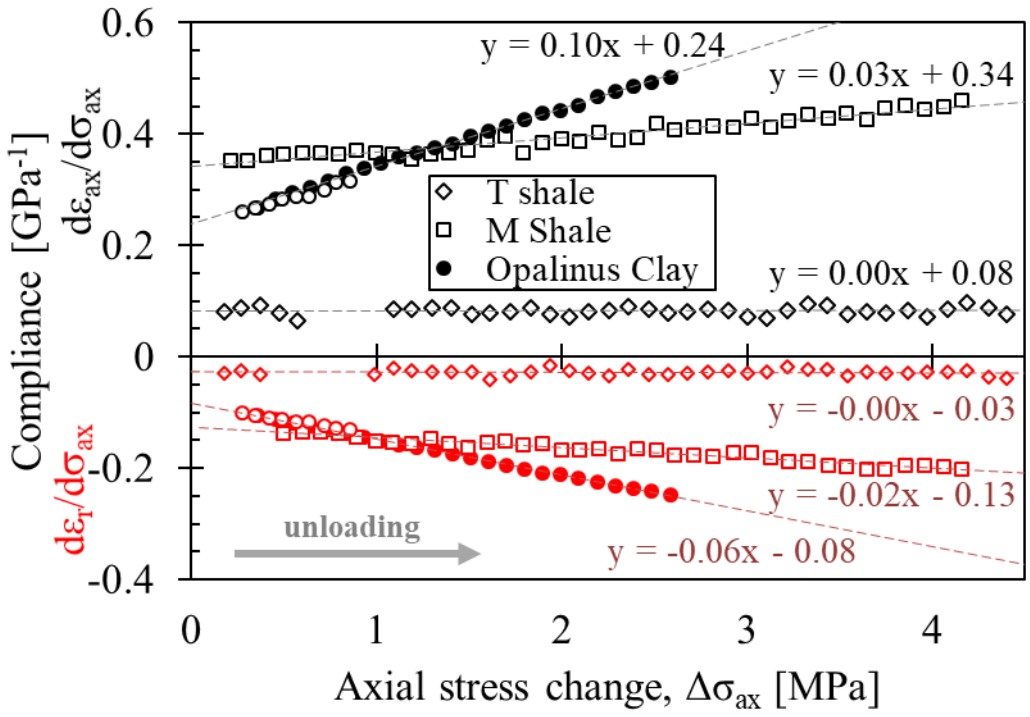

Figure 6. Axial and radial local compliances ($d\varepsilon/d\sigma_{ax}$) plotted as functions of axial stress change ($\Delta\sigma_{ax}$) for T, M shales and Opalinus Clay. Data obtained during undrained triaxial unloadings. Triaxial cycle stress amplitudes were 5 MPa for T and M shales. Opalinus Clay was tested for 1 MPa (open circles) and 3 MPa (closed circles) stress changes (see Figure 5 for the stress-strain plot of these triaxial cycles).

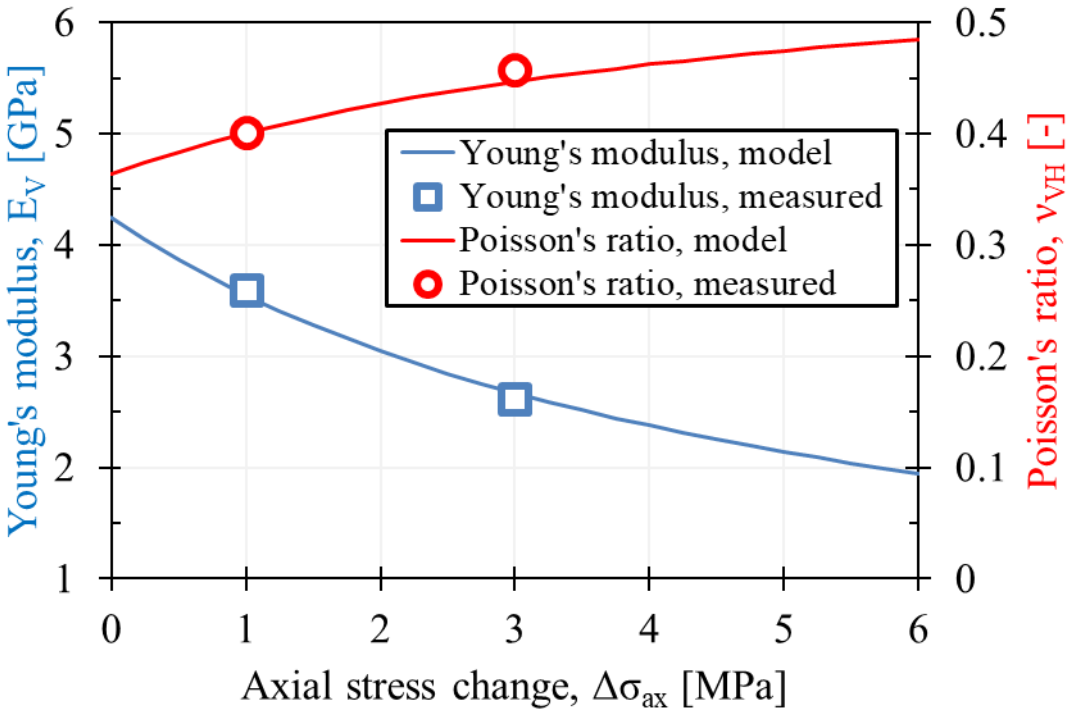

Figure 7. Static Young's modulus and Poisson's ratio as a function of stress amplitude ($\Delta\sigma_{ax}$) for Opalinus Clay. The experimental data (red points) were measured during the unloading sequences of loading-unloading cycles with stress amplitudes of 1 and 3 MPa. The experimental data can well be fit by a simple model that assumes a linear relationship between rock compliance and stress-change amplitude (see Figure 6).

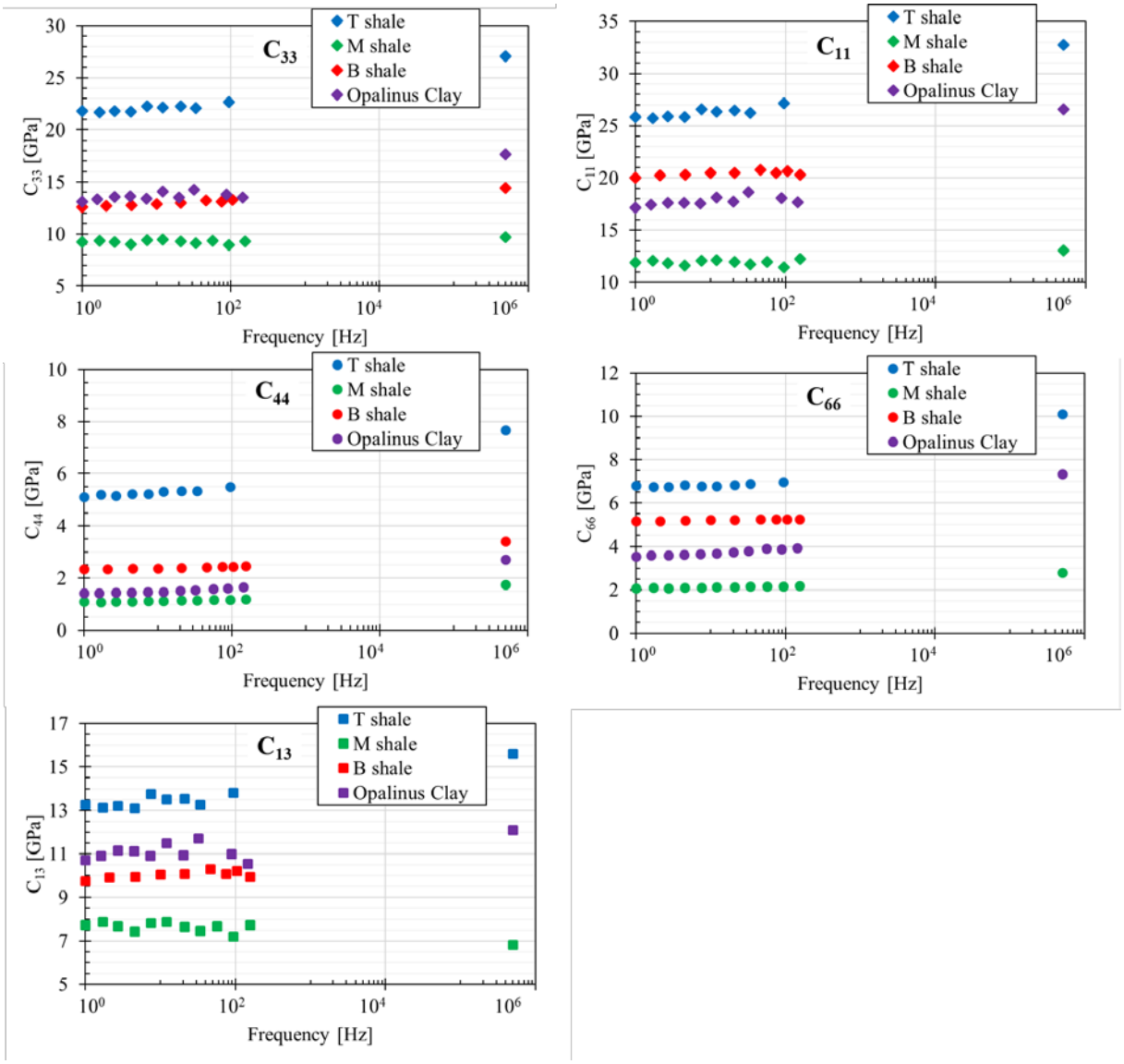

Figure 8. C_{ij} stiffness matrix parameters as functions of frequency for T, M, B, and Opalinus Clay shales measured with low-frequency and ultrasonic techniques. Parameters C_{33} and C_{11} are related to vertical and horisontal P-wave velocities and C_{44} and C_{66} to vertical and in-plane horisontal S-wave velocities, respectively. Ultrasonic parameters C_{11}, C_{66}, and C_{13} were not obtained for B shale.

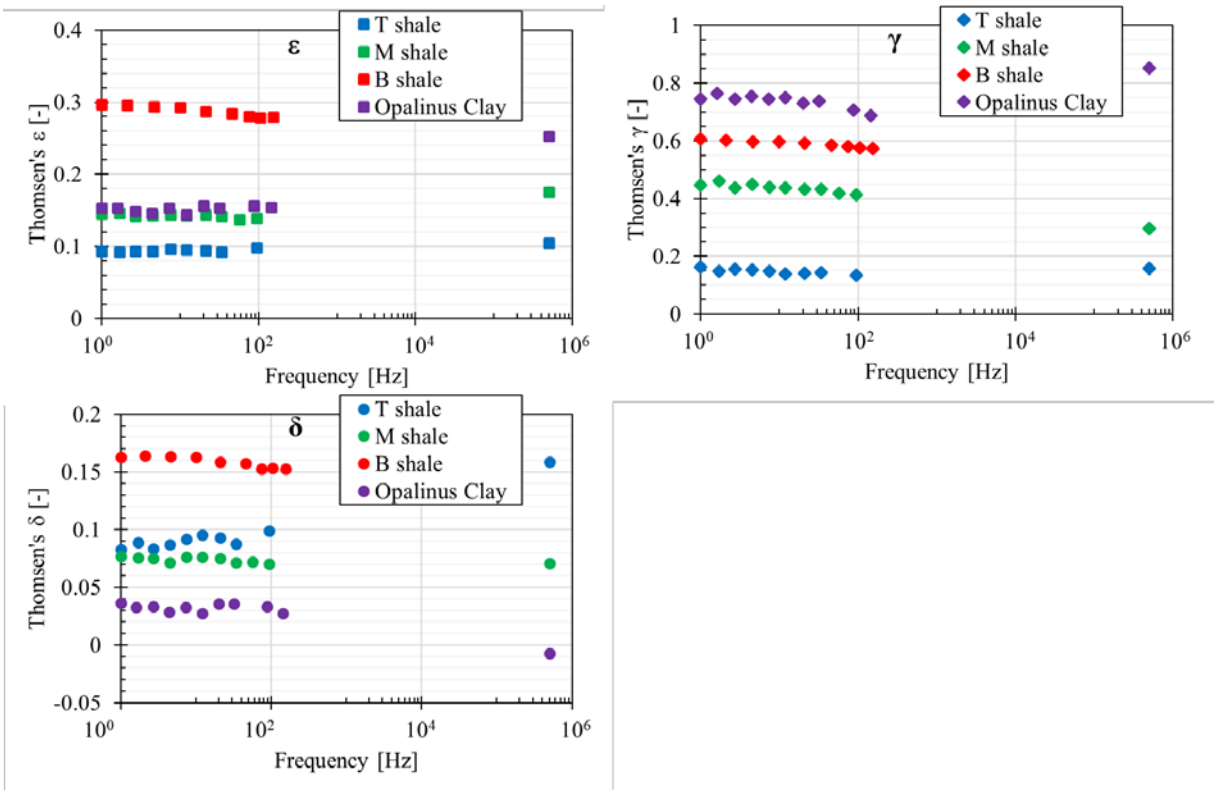

Figure 9. Thomsen anisotropy parameters ε, γ, δ shown as functions of frequency for T, M, B, and Opalinus Clay shales measured with low-frequency and ultrasonic techniques.

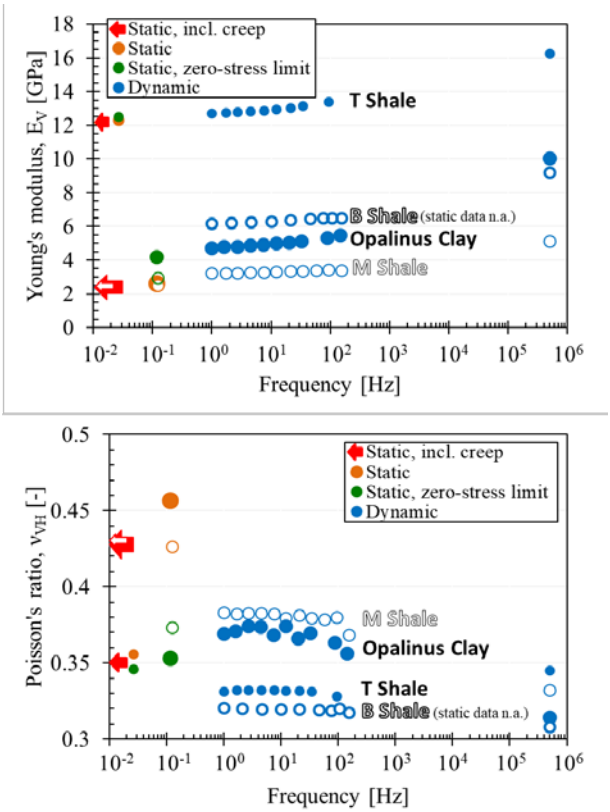

Figure 10. Young's modulus, E_V and Poisson's ratio, ν_{VH} as a function of frequency measured for T, M, B shales and Opalinus Clay. Both low-frequency and ultrasonic dynamic measurements are shown in circles. Static measurements are shown as a frequency that corresponds to strain rates of triaxial tests. All values are taken for unloading parts of undrained static cycles. Squares denote zero-stress extrapolated static stiffness, diamonds denote conventional average stiffness, arrows pointing towards zero frequency represent static stiffness that includes plastic creep deformations after completion of unloading. Note that static properties were not tested for B shale and that ultrasonic elastic parameters for B shale are derived under a certain assumption and may include larger errors than described in the text.

Tables

Table 1. Properties of tested T, M, B and Opalinus Clay shales. The depth of T shale is given with reference to the sea level. Axial stress (σ_{ax}), radial stress (σ_r) and pore pressure (P_f) represent in-situ net stress conditions in the laboratory tests.

	T shale	M shale	B shale	Opalinus Clay, shaly facies
Density [g/cm^3]	2.50	2.01	2.25	2.45
Porosity [%]	15	36	24	15
Clay content [wt%]	57	68	76	66
Age	Middle Miocene	n/a	n/a	Middle Jurassic
Depth	6417 m	n/a	n/a	280 m
σ_{ax} [MPa]	26	12.1	14.9	7
σ_r [MPa]	22	10.7	12.4	7
P_f [MPa]	2	2	2	3

Table 2. Measurement types performed in the low-frequency cell for this study.

Measurement type	Frequency	Strain amplitude (maximum)	Measured parameters
Static (undrained)	Strain rate corresponds to sub-Hz frequency	Order of 10^{-3} m/m	K, E, ν
Low frequency	0.5-150 Hz	$\leq 10^{-6}$ m/m	E, ν
Ultrasonic	500 kHz	~10^{-7} m/m	P- and S-wave velocities

Table 3. Summary of Young's moduli and Poisson's ratios shown in Figure 10 and the ratios between different types of measurements.

Frequency	T shale		M shale		B shale		Opalinus Clay	
	E_V [GPa]	ν_{VH} [-]	E_V [GPa]	ν_{VH} [-]	E_V [GPa]	ν_{VH} [-]	E_V [GPa]	ν_{VH} [-]
Static	12.30	0.36	2.50	0.43	-	-	2.61	0.46
Static, zero-stress limit	12.50	0.35	2.93	0.37	-	-	4.21	0.35
Seismic 1 Hz	12.72	0.33	3.21	0.38	6.19	0.32	4.73	0.37
12 Hz	12.94	0.33	3.31	0.38	6.30	0.32	4.99	0.37
~100 Hz	13.39	0.33	3.41	0.38	6.50	0.32	5.51	0.36
Ultrasonic 500 kHz	16.29	0.35	5.14	0.33	9.20	0.31	10.05	0.31
					Ratios			
Seismic$_{@1\ Hz}$/Static	1.03	0.93	1.29	0.90	-	-	1.81	0.81
Ultrasonic/Seismic$_{@1\ Hz}$	1.28	1.04	1.60	0.87	1.49	0.96	2.12	0.85
Ultrasonic/Static	**1.32**	**0.97**	**2.06**	**0.78**	**-**	**-**	**3.85**	**0.69**

Table 4. Summary of measured velocities and the differences (in %) between seismic and ultrasonic velocities.

Velocity	Frequency			Difference [%]
[m/s]	1 Hz	~100 Hz	500 kHz	1 Hz/500 kHz
T shale				
V_{PH}	3217	3297	3621	13
V_{PV}	2954	3015	3293	11
V_{SV}	1433	1484	1754	22
V_{SH}	1650	1671	2012	22
V_{P45}	3082	3160	3497	13
M shale				
V_{PH}	2434	2388	2550	5
V_{PV}	2144	2112	2195	2
V_{SV}	738	766	935	27
V_{SH}	1015	1036	1179	16
V_{P45}	2264	2224	2333	3
B shale				
V_{PH}	2983	3027	-	-
V_{PV}	2363	2426	2529	7
V_{SV}	1020	1043	1230	21
V_{SH}	1518	1529	-	-
V_{P45}	2637	2690	-	-
Opalinus Clay				
V_{PH}	2643	2714	3293	25
V_{PV}	2311	2369	2683	16
V_{SV}	763	810	1051	38
V_{SH}	1203	1258	1729	44
V_{P45}	2425	2486	2867	18

List of figures

List of tables